

Cite this: *Dalton Trans.*, 2013, **42**, 6603

Comparative study of structures, thermal stabilities and dielectric properties for a ferroelectric MOF [Sr(μ -BDC)(DMF)] $_{\infty}$ with its solvent-free framework†

Ping-Chun Guo,^{a,b} Zhenyu Chu,^a Xiao-Ming Ren,^{*a,b} Wei-Hua Ning^{a,b} and Wanqin Jin^{*a}

A ferroelectric MOF with a formula [Sr(μ -BDC)(DMF)] $_{\infty}$ (**1**) was transformed into [Sr(μ -BDC)(CH₂Cl₂) $_{x}$] $_{\infty}$ (**2**) using a solvent exchange approach, where DMF = *N,N*-dimethylformamide and BDC²⁻ = benzene-1,4-dicarboxylate. The lattice solvents, CH₂Cl₂ molecules, in **2** were removed by heating to give the solvent-free metal-organic framework [Sr(μ -BDC)] $_{\infty}$ (**3**) and the crystal-to-crystal transformation is reversible between **1** and **3**. The release of DMF molecules from **1** results in the metal-organic framework of [Sr(μ -BDC)] $_{\infty}$ expanding a little along the *a*- and *b*-axes. The crystal structure optimizations for **1** and **3** disclosed that the lattice expansion is associated with the alternations of the bond distances and angles in the Sr²⁺ ion coordination sphere along the *a*- and *b*-axes directions. The metal-organic framework **3** collapses at temperatures of more than 600 °C; such an extremely high thermal stability is related to the closed-shell electronic structure of the Sr²⁺ ion, namely, the coordinate bond between the closed-shell Sr²⁺ ion and the bridged BDC²⁻ ligands does not have a preferred direction, which is favored for reducing lattice strains and is responsible for the higher thermal stability. The comparative investigations for the dielectric and ferroelectric behaviors of **1** and **3** confirmed that the motion of the polar DMF molecules, but not the [Sr(μ -BDC)] $_{\infty}$ framework, is responsible for the ferroelectric properties of **1**.

Received 1st December 2012,
Accepted 18th February 2013

DOI: 10.1039/c3dt32880e

www.rsc.org/dalton

1. Introduction

With the development of the electronic and information industry, dielectrics (especially ferroelectric materials) have been widely used in technologically important fields, such as capacitors, resonators and other key components in microwave communication systems and in information storage devices.¹ Thus, research on new ferroelectric and the corresponding dielectric materials has attracted more and more interest in recent years. However, the design and oriented synthesis of these technologically important materials remain a big challenge.^{2,3}

Most of the excellent ferroelectric/special dielectric materials are still traditional inorganic materials, such as ceramics, inorganic salts and their derivatives. To date, studies on metal-organic frameworks (MOFs) or porous coordination polymers (CPs) as ferroelectric/special dielectric materials have

remained sparse. At the end of the 1960s, Okada and Sugie reported the first antiferroelectric MOF, comprised of Cu-(HCOO)₂·4H₂O, with protonated organic amines and formic acid as the templates and building blocks, respectively,⁴ and this MOF has shown an antiferroelectric transition at 227 K. Unfortunately, such a fascinating finding has not attracted enough attention in the exploration of dielectric MOFs/CPs materials for nearly 40 years. MOFs/CPs have been rapidly developed owing to the potential applications in the fields of selective gas separation and storage,⁵ molecular sensing,⁶ catalysis⁷ and luminescence materials⁸ since the 1990s. Besides the properties mentioned above, additional functional properties of the MOF/CP materials have been explored, which include the proton conductivity,⁹ electronic transport behavior,¹⁰ dielectric property¹¹ and magnetic property^{12,13}. For instance, Kobayashi and coworkers reported three MOFs, [Mn₃(HCOO)₆](H₂O)(CH₃OH), [Mn₃(HCOO)₆](C₂H₅OH)¹⁴ and [La₂Cu{NH(CH₂COO)₂}]₆(H₂O)_{*n*},¹⁵ where the movable polar guest or solvent molecules show an intriguing ferroelectricity and paraelectric-to-ferroelectric transitions that are induced by the ordering or freezing of the polar guest molecules. A MOF with a formula of [(CH₃)₂NH₂]Zn(HOOC)₃ and Perovskite structure¹⁶ displays antiferroelectric behavior due to the electric ordering of the organic cations. Besides, the ferroelectric MOF

^aState Key Laboratory of Materials-Oriented Chemical Engineering, Nanjing University of Technology, Nanjing 210009, P. R. China. E-mail: xmren@njut.edu.cn, wqjin@njut.edu.cn; Fax: +86 25 58139481; Tel: +86 25 58139476

^bCollege of Science, Nanjing University of Technology, Nanjing 210009, P. R. China

†Electronic supplementary information (ESI) available. See DOI: 10.1039/c3dt32880e

$[\text{NH}_4]\text{Zn}(\text{HCOO})_3$ ¹⁷ and a series of multiferroic MOFs with general formula $[(\text{CH}_3)_2\text{NH}_2]\text{M}(\text{HCOO})_3$ ¹⁸ or $[\text{NH}_4]\text{M}(\text{HCOO})_3$ ¹⁹ where M = Mn, Fe, Co and Ni, were discovered by different research groups, respectively.

In this content, we recently reported that a highly thermal stable MOF compound, $[\text{Sr}(\mu\text{-BDC})(\text{DMF})]_\infty$ (**1**) (DMF = *N,N*-dimethylformamide; BDC²⁻ = benzene-1,4-dicarboxylate), showed ferroelectricity.²⁰ To better understand this issue, a comparative investigations of the structure, ferroelectric and dielectric properties of **1** with the corresponding solvent-free compound were completed, and the results are presented in this paper.

2. Experimental

2.1. Materials and chemicals

All commercially available chemicals $[\text{Sr}(\text{NO}_3)_2]$ and H_2BDC and solvents (DMF and CH_2Cl_2) were of reagent grade and used as received without further purification.

2.2. Sample preparation

$[\text{Sr}(\mu\text{-BDC})(\text{DMF})]_\infty$ (**1**) was prepared following the procedure in a published paper.²⁰ The sample exchanged by dichloromethane, $[\text{Sr}(\mu\text{-BDC})(\text{CH}_2\text{Cl}_2)_x]_\infty$ (**2**), was obtained by soaking **1** in dichloromethane for 24 h and then refreshing the dichloromethane three times. The activated solvent-free compound $[\text{Sr}(\mu\text{-BDC})]_\infty$ (**3**) was prepared by heating at 130 °C under vacuum overnight. The sample of solvent-free **3** was re-immersed in DMF to give sample **4**.

2.3. Physical measurements

Power X-ray diffraction (PXRD) data were collected on a Bruker D8 diffractometer with Cu K α radiation ($\lambda = 1.54018 \text{ \AA}$). TGA experiments were performed with a STA449 F3 thermogravimetric analyzer in the 30–800 °C range at a warming rate of 10 °C min⁻¹ under a nitrogen atmosphere and the polycrystalline samples were placed in an Al₂O₃ crucible. The powdered samples of **1** and **3** were pressed into a pellet under the pressure of *ca.* 10 MPa with a thickness of *ca.* 0.87 mm, 0.83 mm for **1** and **3**, respectively; the area of **1** and **3** is 7.06 mm². Two opposite surfaces of the pellets were covered with a gold film *via* vacuum coating. The measurements of the temperature and frequency dependent dielectric constant and loss were carried out by employing a Concept 80 system (Novo-control, Germany) in the temperature range 0–277 °C (273–450 K). The powdered pellets of **1** and **3** were sandwiched by two copper electrodes and the ac frequencies spanned from 1 to 10⁷ Hz. The dielectric hysteresis loop measurements were carried out on a ferroelectric tester (Radiant Technology) and the ac electric field frequency ranged from 10 to 1000 Hz, the pellets covered with a gold film were sandwiched by the copper electrodes and immersed in insulating oil while measured.

Low-pressure gas sorption measurements: glass sample tubes of a known weight were loaded with approximately

200 mg of the sample, and sealed using a TranSeal. Samples were degassed at 150 °C for 24 h on a Micromeritics ASAP 2020 analyzer until the outgas rate was no more than 1 mTorr min⁻¹. The degassed sample and sample tube were weighed precisely and then transferred back to the analyzer (with the TranSeal preventing exposure of the sample to the air after degassing). The outgas rate was again confirmed to be less than 1 mTorr min⁻¹. Adsorption isotherms were measured at 77 K in a liquid nitrogen bath for N₂. The isotherm for the adsorption and desorption of N₂ on activated **3** at 77 K and the pore size distribution are shown in Fig. S1.†

2.4. Details for crystal structure optimization

The crystal structure calculations presented were performed in the density functional theory (DFT) framework. The starting crystal structures of **1** and **3** for optimization were taken from the X-ray single crystal structure of **1** at 293 K. The Cambridge sequential total energy package (CASTEP) module²¹ was employed in the calculations. The total plane-wave pseudo-potential method forms the basis of the CASTEP calculations. The exchange-correlation effects were treated within the generalized gradient approximation (GGA) with the Perdew–Burke–Ernzerhof functional.²² The plane-wave basis set energy cutoff was set at 300 eV for **1** and **3**. The convergence parameters were as follows: the SCT tolerance 2×10^{-6} eV per atom, the total energy tolerance 2×10^{-5} eV per atom, the maximum force tolerance 0.05 eV Å⁻¹, the maximum stress component 0.1 GPa and the displacement of convergence tolerance 0.002 Å. All above limits can accurately constrain the simulative process to end at the stable constructions of **1** and **3**.

3. Results and discussion

3.1. Crystal to crystal transformation between **1** and **3**

The detailed crystal structure of **1** was reported in our previous work,²⁰ herein, a simple description is given to assist us for better understanding the corresponding discussion in the next sections. The three-dimensional (3-D) framework of **1** is built by Sr²⁺ ions and BDC²⁻ bridged ligands and an asymmetric unit comprised of one Sr²⁺, one BDC²⁻ together with one DMF molecule; the coordination sphere of the Sr²⁺ ion (a distorted bicapped coordination octahedron) and the packing diagram projected along the *c*-axis direction are displayed in Fig. 1a

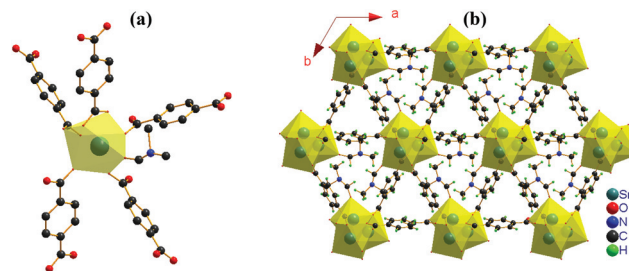


Fig. 1 (a) Coordination sphere of Sr²⁺ ion where H atoms were omitted for clarity, (b) packing diagram viewed along the *c*-axis in the crystal of **1**.

and b, respectively. Two types of triangle channels appear in MOF **1**, the smaller one is empty and the larger channel is filled by DMF molecules that are bound directly to the Sr²⁺ ions.

The DMF molecules, bound to the Sr²⁺ ions in the channels of crystal **1**, can be removed to give the solvent-free compound **3**, by heating at *ca.* 265 °C or using dichloromethane exchange. As shown in Fig. 2, all diffraction peaks are broadened and the diffraction with the Miller index (*h k l*) = (1 0 0) is shifted faintly to the lower angle side of the PXRD profile of **3** (with $2\theta = 9.6288^\circ$), compared to that of **1** (with $2\theta = 9.3266^\circ$), indicating that DMF molecule removal from the channels of **1** results in reduced crystallinity of the metal-organic framework and the lattice slightly expands along the *a*- and *b*-axes. It is noted that **3** can be transformed into **1** by re-immersing **3** in DMF. This observation demonstrates the crystal-to-crystal transformation is reversible between **1** and **3**.

Generally, lattice shrinking is observed when the lattice solvents inside the metal-organic framework are removed. In contrast to the common situation, the *a*- and *b*-axes slightly expand with **1** losing solvents in the channels to transform into **3**. It is unavailable to determine the X-ray single crystal structure of **3** owing to its bad crystallinity. In order to gain deeper insight into this anomalous structural change, the crystal structure optimizations were performed for **1** and **3**.

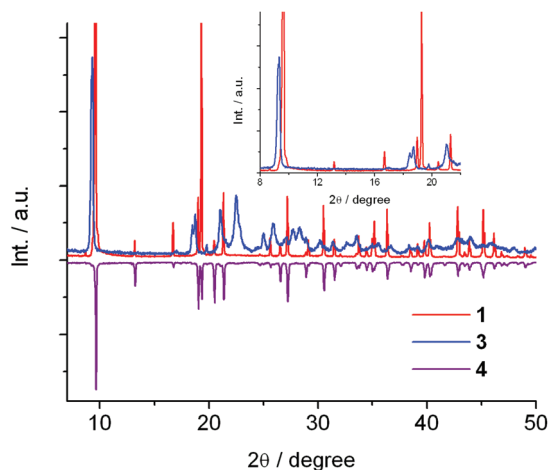


Fig. 2 PXRD profiles where the red, blue and purple lines correspond respectively to the patterns of **1**, **3** and **4**.

The lattice parameters, as well as the bond distances and angles in the coordination sphere of the Sr²⁺ ion, obtained from both the X-ray single crystal structure analyses and the crystal structure optimization, are summarized in Tables 1 and 2 for **1** and **3**, respectively. The DMF and BDC²⁻ molecule structures and their bond distances in the crystal of **1**, obtained from the single crystal structure analysis at 293 K and the crystal structure optimization, are shown in Fig. S2.†

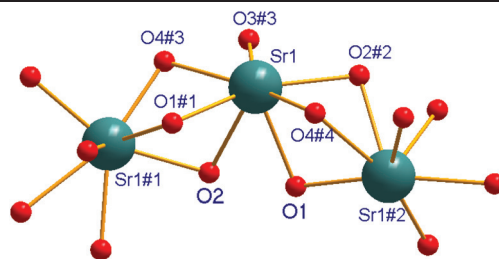
The lattice parameters exhibit slight expansion in the optimized crystal structure compared to the single crystal analysis for **1** (see Table 1). As illustrated in Fig. 3 and Table 2, most of the bond distances and angles in the Sr²⁺ ion coordination sphere are in agreement, and fall well between the single crystal structure at 293 K and the optimized structure for **1**, except the bond distances $d(\text{Sr1-O1}) = 2.679 \text{ \AA}$ (2.824 Å) and $d(\text{Sr1-O4\#3}) = 2.767 \text{ \AA}$ (3.052 Å), and bond angles $\angle\text{O1-Sr1-O3\#3} = 99.8^\circ$ (103.6°), $\angle\text{O2-Sr1-O2\#2} = 111.4^\circ$ (108.0°), $\angle\text{O3\#3-Sr1-O4\#4} = 147.8^\circ$ (151.3°) and $\angle\text{O1\#1-Sr1-O3\#3} = 124.2^\circ$ (119.5°) in the single crystal structure (the optimized crystal structure), where the hash-marked atoms are generated by a symmetric operation with the symmetric codes: #1 = $-x + y, 1 - x, -1/3 + z$; #2 = $1 - y, 1 + x - y, 1/3 + z$; #3 = $1 - x + y, 2 - x, -1/3 + z$ and #4 = $-1 + x, y, z$. It is worthy of note that the bond lengths in the BDC²⁻ moiety are quite close to each other between the optimized and the single crystal structures (ref. Fig. S2.†).

Upon comparison of the optimized crystal structures of **1** and **3**, it was found that the *a*- and *b*-axes expand a little while the *c*-axis shrinks slightly after the DMF molecules in the channels are removed (ref. Table 1), and the lattice parameter alternations stem from the coordination sphere change of the Sr²⁺ ion along the *a*- and *b*-axes. For instance, the significant changes in the coordination sphere of the Sr²⁺ ion between **1** and **3** concerns the bond distances and angles below, $d(\text{Sr1-O1}) = 2.824 \text{ \AA}$ (2.694 Å), $d(\text{Sr1-O4\#3}) = 3.052 \text{ \AA}$ (3.217 Å), $\angle\text{O1-Sr1-O4\#4} = 78.9^\circ$ (86.5°), $\angle\text{O1-Sr1-O3\#3} = 103.6^\circ$ (120.7°), $\angle\text{O2-Sr1-O3\#3} = 81.5^\circ$ (92.8°), $\angle\text{O2-Sr1-O2\#2} = 108.0^\circ$ (112.1°), $\angle\text{O2-Sr1-O4\#4} = 117.3^\circ$ (123.7°), $\angle\text{O1\#1-Sr1-O3\#3} = 119.5^\circ$ (112.3°), $\angle\text{O4\#4-Sr1-O4\#3} = 161.5^\circ$ (155.5°), $\angle\text{O3\#3-Sr1-O2\#2} = 82.3^\circ$ (92.3°), $\angle\text{O3\#3-Sr1-O4\#4} = 151.3^\circ$ (143.5°) in **1** (**3**). Obviously, the significant increase of the bond distance Sr1-O4#3 and the angle $\angle\text{O1-Sr1-O3\#3}$, from **1** to **3**, is responsible for the *a*- and *b*-axes expansion.

Table 1 Lattice parameters for **1** and **3**^a

	1		3		
	<i>T</i> = 243 K	<i>T</i> = 293 K	<i>T</i> = 403 K	Optimization	Optimization
<i>a</i> /Å	10.6123(2)	10.62017(15)	10.6396(3)	10.8133	10.8427
<i>b</i> /Å	10.6123(2)	10.62017(15)	10.6396(3)	10.8133	10.8427
<i>c</i> /Å	9.8289(2)	9.84171(14)	9.8731(3)	10.0866	10.0379
<i>V</i> /Å ³	958.64(3)	961.31(2)	967.90(5)	1021.39	1021.99

^a The lattice parameters of **1** from the X-ray single crystal structure analyses at 243, 293 and 403 K are cited from the literature.²⁰

Table 2 Bond distances (Å) and angles (°) in the coordination sphere of the Sr²⁺ ion for **1** and **3**^a

	1			Optimization	3
	<i>T</i> = 243 K	<i>T</i> = 293 K	<i>T</i> = 403 K		Optimization
d(Sr1–O1)	2.679	2.679	2.679	2.824	2.694
d(Sr1–O2)	2.713	2.714	2.723	2.749	2.612
d(Sr1–O1#1)	2.527	2.534	2.547	2.562	2.564
d(Sr1–O2#2)	2.557	2.562	2.581	2.615	2.580
d(Sr1–O3#3)	2.550	2.551	2.550	2.664	2.562
d(Sr1–O4#3)	2.758	2.767	2.779	3.052	3.217
d(Sr1–O4#4)	2.500	2.498	2.495	2.516	2.451
∠O1–Sr1–O2	48.2	48.1	47.8	47.4	49.8
∠O1–Sr1–O4#4	77.4	77.7	78.2	78.9	86.5
∠O1–Sr1–O2#2	71.7	71.6	71.4	70.1	70.4
∠O1–Sr1–O3#3	99.5	99.8	99.7	103.6	120.7
∠O1–Sr1–O4#3	109.0	108.8	108.4	107.4	108.1
∠O1–Sr1–O1#1	97.1	97.0	96.9	96.8	98.5
∠O2–Sr1–O1#1	71.6	71.5	71.2	72.1	71.9
∠O2–Sr1–O4#3	69.5	63.4	63.4	62.1	60.8
∠O2–Sr1–O3#3	81.3	81.7	81.8	81.5	92.8
∠O2–Sr1–O2#2	111.4	111.4	111.1	108.0	112.1
∠O2–Sr1–O4#4	116.1	116.2	116.2	117.3	123.7
∠O1#1–Sr1–O4#3	75.6	75.6	75.5	74.0	74.3
∠O1#1–Sr1–O3#3	124.3	124.2	123.9	119.5	112.3
∠O1#1–Sr1–O2#2	156.1	156.0	155.9	157.4	155.1
∠O1#1–Sr1–O4#4	87.8	87.7	87.8	88.1	84.3
∠O4#3–Sr1–O3#3	48.8	48.7	48.5	45.6	43.6
∠O4#3–Sr1–O2#2	127.8	127.8	127.8	126.8	129.9
∠O4#4–Sr1–O4#3	162.6	162.6	162.6	161.5	155.5
∠O3#3–Sr1–O2#2	79.1	79.3	79.6	82.3	92.3
∠O3#3–Sr1–O4#4	147.7	147.8	148.0	151.3	143.5
∠O2#2–Sr1–O4#4	69.4	69.4	69.4	71.6	73.1

^a Symmetric codes: #1 = $-x + y, 1 - x, -1/3 + z$; #2 = $1 - y, 1 + x - y, 1/3 + z$; #3 = $1 - x + y, 2 - x, -1/3 + z$; #4 = $-1 + x, y, z$.

3.2. Thermal stabilities of **1** and **3**

The TG plots of **1–4** are displayed in Fig. 4. The DMF molecules bound to the Sr²⁺ ions in the channels of **1** were completely released at *ca.* 265 °C, this temperature is much higher than the DMF decomposition temperature (151 °C). Interestingly, although the PXRD profiles are almost the same for **1** and **4**, the TG plots show distinctions from each other. The DMF molecules begin to become lost below ~100 °C in **4**, but the temperature to achieve full DMF molecule removal is the same as that for **1**. In addition, the thermal stability of the metal–organic framework after the DMF molecules were removed is higher in **4** than in **1**. For **2**, the dichloromethane molecules inside the channels of the framework are lost between 65 and 110 °C, and this temperature is much lower than the temperature of DMF release since CH₂Cl₂ is a weakly coordinating solvent compared to DMF. The total weight loss is 12% for the lattice solvents in **2**, and this value is only close

to one half when the calculation is based on the formula [Sr(BDC)(CH₂Cl₂)]_∞. For solvent-free **3**, no sizable weight loss was detected before the metal–organic framework collapsed.

It is worthy of note that the thermal stability of the solvent-free framework for samples **2–4** is much higher compared to the as-synthesized sample **1**. This phenomenon is probably related to the fact that the blast of large amounts of gas, stemming from the DMF decomposition, reduces the thermal stability of the framework in **1** with high crystallinity. Another interesting issue is that the frameworks in **2–4** can be thermally stable at more than 600 °C. To date, a large number of MOFs have been reported, it was noted that the natures of both the metal ions and bridged ligands affect strongly the thermal stability of a MOF compound, in general, the MOF constructed from the flexible linkers is more thermally stable than one built from rigid linkers. In addition, MOFs with a main group metal ion or d¹⁰ transition metal ion are more thermally stable than those with open-shell transition metal

ions. The relationship between the electronic configuration of the Sr^{2+} ion and the thermal stability of the corresponding MOF can be understood, since the coordinate bond between the closed-shell metal ion and ligands does not have a preferred direction; such a type of bond is favored for reducing lattice strains, to give the corresponding MOF possessing higher thermal stability.

3.3. Ferroelectricity of 1 and 3

The crystals of 3, obtained from the removal of DMF from the crystals 1, are much more easily broken, even if they retain the original shape; as a result, it was not possible to measure the P - E plot using a single crystal of 3. The field dependence of polarization was only investigated using the powdered sample of 3. The P - E plots for the powdered samples of 1 and 3 are displayed in Fig. 5, and the typically ferroelectric hysteresis loops appear in the powdered sample of 1, while they were not clear in the powdered sample of 3. The spontaneous

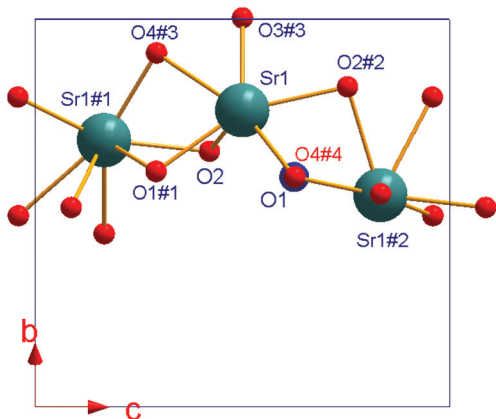


Fig. 3 Structure for illustrating the changes of both the Sr^{2+} ion coordination sphere and the crystallographic a - and b -axes (the hash marked atoms are generated by a symmetric operation with the symmetric codes: #1 = $-x + y, 1 - x, -1/3 + z$; #2 = $1 - y, 1 + x - y, 1/3 + z$; #3 = $1 - x + y, 2 - x, -1/3 + z$ and #4 = $-1 + x, y, z$).

polarization (P_s), remnant polarization (P_r) and coercive field (E_c) are roughly estimated as $0.025 \mu\text{C cm}^{-2}$, $0.018 \mu\text{C cm}^{-2}$, and 7.1 kV cm^{-1} under an applied field of 14.5 kV cm^{-1} with an ac frequency (f) of 16.7 Hz for 1; these values are less than the corresponding parameter values obtained from the single crystal sample of 1 along the polar c -axis direction.²⁰ This observation is due to the existence of highly anisotropic polarization in the ferroelectric material.

A ferroelectric hysteresis loop demonstrates that the macroscopic polarization in the ferroelectric material is reversed or switched under an ac applied electric field, and the macroscopic polarization reversal originates from the local, microscopic polarization reversal, which includes electronic, atomic and ionic displacement polarization reversals as well as permanent dipole reversal under an ac electric field. In our previous study,²⁰ two possible mechanisms for the polarization reversal were proposed according to the analyses of the variable-temperature single crystal structures, namely, the swing motion of the polar DMF molecule bound to the Sr^{2+} ion along the c -axis direction, as well as the deformation of the Sr^{2+} coordination sphere, arising from the DMF displacement along the Sr-O (DMF) bond direction. From the P - E measurements of 1 and

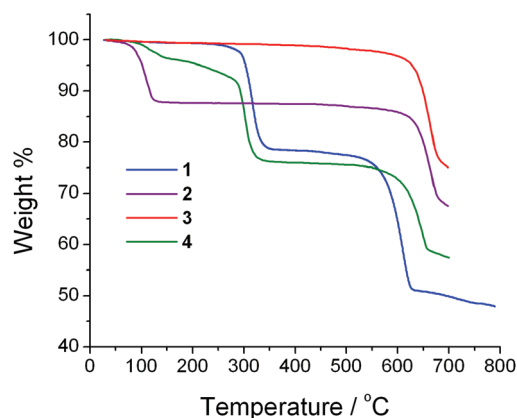


Fig. 4 TG plots of 1–4 at a warm rate of 10 °C min^{-1} , respectively.

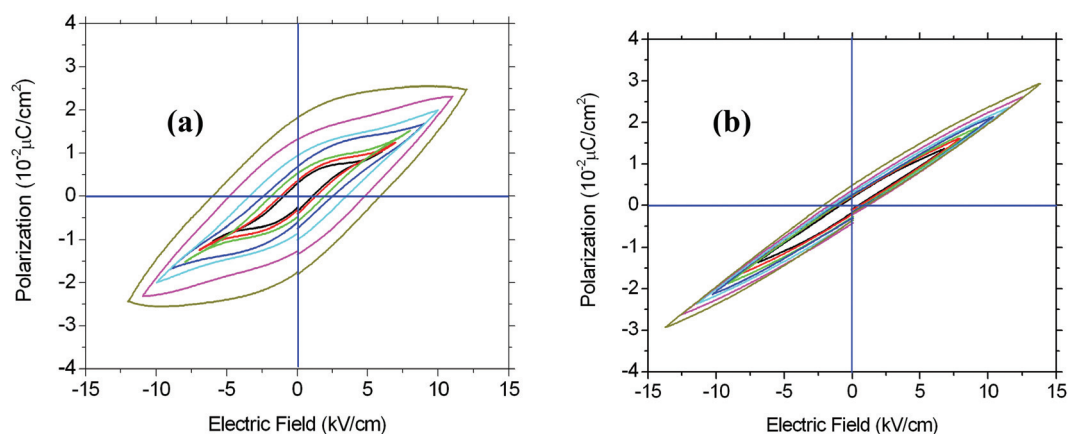


Fig. 5 Plots of polarization versus electric field of (a) 1 and (b) 3 at ambient temperature.

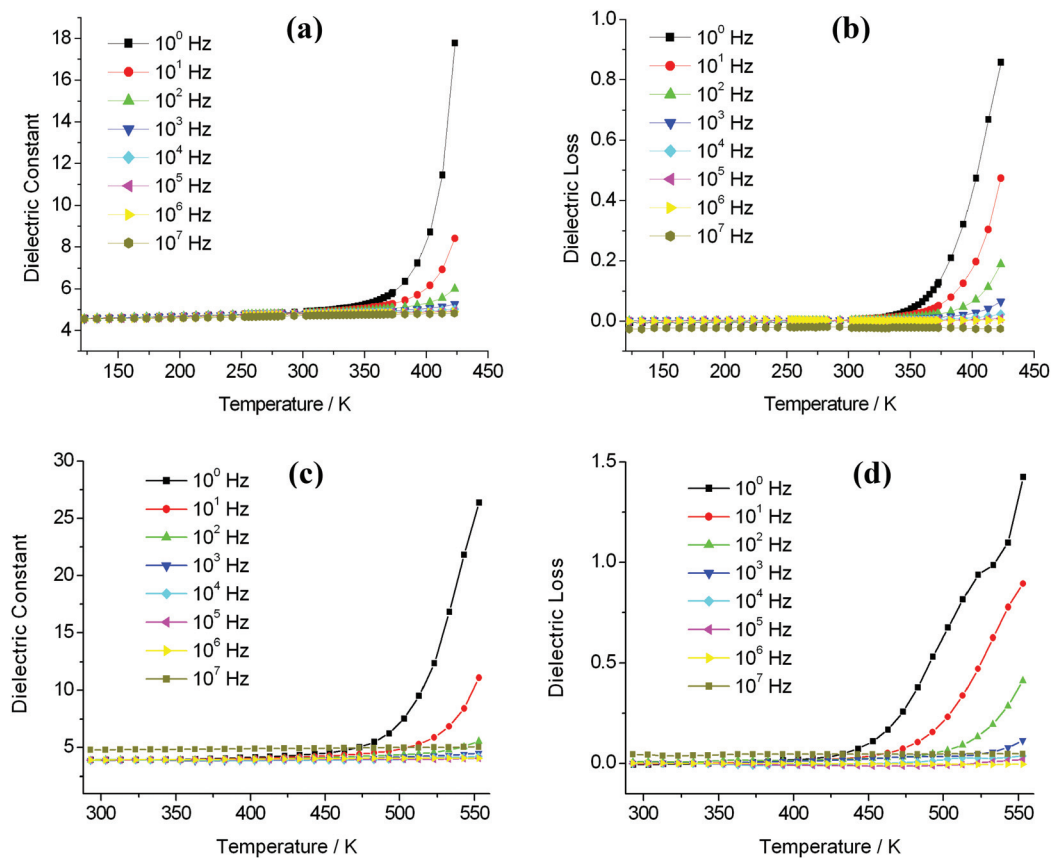


Fig. 6 Temperature dependencies of the dielectric constant, ϵ' , and dielectric loss, $\tan(\delta)$, of (a, b) **1** and (c, d) **3** in the frequency range 1– 10^7 Hz.

3, it is obvious that the motion of the polar DMF molecules really plays a crucial role in the process of macroscopic polarization reversal and the framework is not responsible for the ferroelectric behavior of **1**.

3.4. Dielectric properties of **1** and **3**

The dielectric behavior of **3** was further investigated and compared with that of **1** in the frequency range 1– 10^7 Hz. The dielectric constant, ϵ' , and dielectric loss, $\tan(\delta)$, as a function of temperature for **1** and **3** are displayed in Fig. 6, respectively. The ϵ' and $\tan(\delta)$ values are nearly constant below 325 K for **1**, with $\epsilon' \approx 5.04$ and $\tan(\delta) \approx 0.002$, and at 460 K for **3**, with $\epsilon' \approx 4.96$ and $\tan(\delta) \approx 0.041$. Both the dielectric constant and loss rise rapidly with increasing of the temperature above 325 K for **1** and 460 K for **3**, especially, under a lower frequency ($f < 10^4$ Hz). The frequency-dependent behavior of the ϵ' and $\tan(\delta)$ values indicated the presence of dielectric relaxation in the higher temperature region. The distinctions of the dielectric properties are observed between **1** and **3**, for example, (1) $\epsilon' \approx 18$ for **1**, while $\epsilon' \approx 4.9$ for **3** at 433 K under $f = 1$ Hz. (2) The $\tan(\delta)$ value increases monotonically with temperature for **1**, whereas shoulder is shown for **3**. These differences demonstrated that **1** and **3** possess dissimilar dielectric relaxation behaviors, which are further identified from the different frequency dependencies of ϵ' and $\tan(\delta)$ for **1** and **3** at various temperatures (see Fig. 7).

In the four different dielectric relaxation mechanisms, the one originating from the electronic transitions or the bond vibrations within a molecule appears in the high frequency (f) region with $f > 10^{12}$ Hz, and the dielectric relaxation arising from the dipole motion or ionic polarization occurs in the frequency regime ($f < 10^{10}$ Hz). On the one hand, the variable-temperature single crystal structure analyses indicated that the coordinated DMF molecule is disordered at higher temperature; on the other hand, the Sr^{2+} ion is bound to the O atoms within the coordination sphere, only through electrostatic interactions, owing to the closed-shell electronic configuration of the Sr^{2+} ion. As a result, it is possible that the dipole orientations of the disordered DMF molecules and the SrO_8 coordination polyhedra are changed under an ac electrical field, and the dielectric relaxation observed in the 1– 10^4 Hz frequency range could be attributed to the dipole orientation motions of the DMF molecules and the SrO_8 coordination polyhedra in **1**, while only to the dipole orientation motion of the SrO_8 coordination polyhedra in **3**.

4. Conclusion

In summary, we investigated comparatively the crystal structures, thermal stabilities, ferroelectric and dielectric behaviors of the ferroelectric MOF $[\text{Sr}(\mu\text{-BDC})(\text{DMF})]_{\infty}$ (**1**) and the

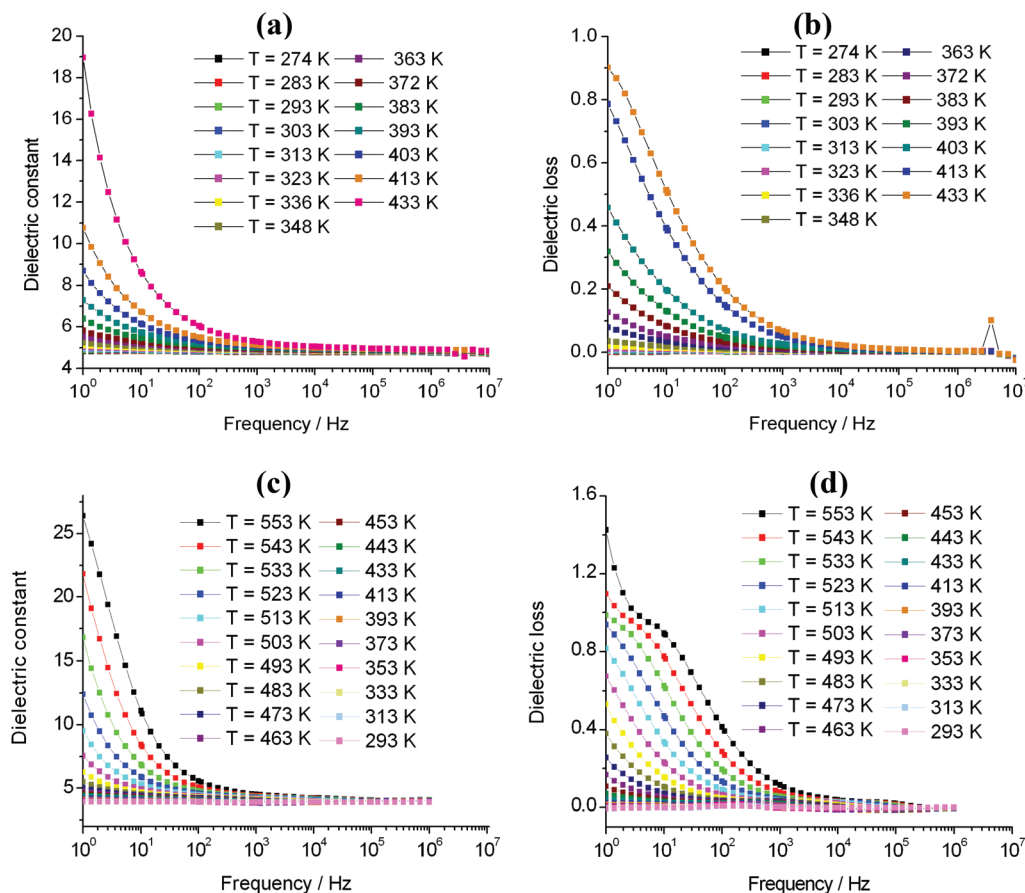


Fig. 7 Frequency dependencies of the dielectric constant, ϵ' , and dielectric loss, $\tan(\delta)$, of (a, b) **1** in the temperature range 274–433 K and (c, d) **3** in the temperature range 293–553 K.

corresponding solvent-free framework $[\text{Sr}(\mu\text{-BDC})]_{\infty}$ (**3**). A reversible crystal-to-crystal transformation occurs between **1** and **3**, and a slight expansion of the lattice a and b parameters is observed, which is associated with the bond distances and angles in the coordination sphere of the Sr^{2+} ion increasing along the a - and b -axes. The solvent-free MOF $[\text{Sr}(\mu\text{-BDC})]_{\infty}$ shows an extremely high thermal stability, which is thought to be related to the closed-shell electronic structure of the Sr^{2+} ion. The coordinate bonds between the Sr^{2+} ion and the O atoms of the BDC^{2-} ligands have no preferred orientation in space, which is favored for reducing lattice strains and is responsible for the higher thermal stability. The ferroelectricity occurs in **1** whereas disappears in **3**, indicating that the motion of the DMF molecules in the channels is responsible for the macroscopic polarization reversal in **1**.

Acknowledgements

Authors thank National Nature Science Foundation of China (grant no. 91122011, 21071080 and 21176115) for financial support.

Notes and references

- (a) T. A. Vanderah, *Nature*, 2002, **298**, 1182–1184; (b) S. Horiuchi and Y. Tokura, *Nat. Mater.*, 2008, **7**, 357–366.
- H. N. Lee, H. M. Christen, M. F. Christen, C. M. Rouleau and D. H. Lowndes, *Nature*, 2005, **433**, 395–399.
- (a) L. Wen, L. Zhou, B. Zhang, X. Meng, H. Qu and D. Li, *J. Mater. Chem.*, 2012, **22**, 22603–22609; (b) C. M. Liu, R. G. Xiong, D. Q. Zhang and D. B. Zhu, *J. Am. Chem. Soc.*, 2010, **132**, 4044–4045.
- K. Okada and H. Sugie, *J. Phys. Soc. Jpn.*, 1968, **25**, 1128–1132.
- D. N. Dybtsev, H. Chun, S. H. Yoon, D. Kim and K. Kim, *J. Am. Chem. Soc.*, 2004, **126**, 32–33; M. Dincă, A. F. Yu and J. R. Long, *J. Am. Chem. Soc.*, 2006, **128**, 8904–8913.
- H. L. Jiang, Y. Tatsu, Z. H. Lu and Q. Xu, *J. Am. Chem. Soc.*, 2010, **132**, 5586–5587.
- P. Y. Wu, C. He, J. Wang, X. J. Peng, X. Z. Li, Y. L. An and C. Y. Duan, *J. Am. Chem. Soc.*, 2012, **134**, 14991–14999; D. B. Dang, P. Y. Wu, C. He, Z. Xie and C. Y. Duan, *J. Am. Chem. Soc.*, 2010, **132**, 14321–14323.
- (a) W. L. Liu, J. H. Yu, J. X. Jiang, L. M. Yuan, B. Xu, Q. Liu, B. T. Qu, G. Q. Zhang and C. G. Yan,

- CrystEngComm*, 2011, **13**, 2764–2773; (b) W. L. Liu, L. H. Ye, X. F. Liu, L. M. Yuan, J. X. Jiang and C. G. Yan, *CrystEngComm*, 2008, **10**, 1395–1403; (c) J. H. Yu, R. Yao, L. M. Yuan, B. Xu, B. T. Qu and W. L. Liu, *Inorg. Chim. Acta*, 2011, **376**, 222–229; (d) W. L. Liu, L. H. Ye, X. F. Liu, L. M. Yuan, X. L. Lu and J. X. Jiang, *Inorg. Chem. Commun.*, 2008, **11**, 1250–1252.
- 9 (a) J. A. Hurd, R. Vaidhyanathan, V. Thangadurai, C. I. Ratcliffe, I. L. Moudrakovski and G. K. H. Shimizu, *Nat. Chem.*, 2009, **1**, 705–710; (b) M. Sadakiyo, T. Yamada and H. Kitagawa, *J. Am. Chem. Soc.*, 2009, **131**, 9906–9907.
- 10 (a) Y. Kobayashi, B. Jacobs, M. D. Allendorf and J. R. Long, *Chem. Mater.*, 2010, **22**, 4120–4122; (b) C. Narayan, T. Miyakai, S. Seki and M. Dincă, *J. Am. Chem. Soc.*, 2012, **134**, 12932–12935.
- 11 (a) T. Okubo, R. Kawajiri, T. Mitani and T. Shimoda, *J. Am. Chem. Soc.*, 2005, **127**, 17598–17599; (b) Q. Ye, Y. M. Song, G. X. Wang, K. Chen, D. W. Fu, P. W. H. Chan, J. S. Zhu, S. P. D. Huang and R. G. Xiong, *J. Am. Chem. Soc.*, 2006, **128**, 6554–6555; (c) Z. Guo, R. Cao, X. Wang, H. Li, W. Yuan, G. Wang, H. Wu and J. Li, *J. Am. Chem. Soc.*, 2009, **131**, 6894–6895.
- 12 (a) G. J. Halder, C. J. Kepert, B. Moubaraki, K. S. Murray and J. D. Cashion, *Science*, 2002, **298**, 1762–1765; (b) G. J. Halder, K. W. Chapman, S. M. Neville, B. Moubaraki, K. S. Murray, J. F. Létard and C. J. Kepert, *J. Am. Chem. Soc.*, 2008, **130**, 17552–17562; (c) S. M. Neville, G. J. Halder, K. W. Chapman, M. B. Duriska, B. Moubaraki, K. S. Murray and C. J. Kepert, *J. Am. Chem. Soc.*, 2009, **131**, 12106–12108; (d) P. D. Southon, L. Liu, E. A. Fellows, D. J. Price, G. J. Halder, K. W. Chapman, B. Moubaraki, K. S. Murray, J. F. Létard and C. J. Kepert, *J. Am. Chem. Soc.*, 2009, **131**, 10998–11009.
- 13 (a) L. Shen, S. W. Yang, S. Xiang, T. Liu, B. Zhao, M. F. Ng, J. Göettlicher, J. Yi, S. Li, L. Wang, J. Ding, B. Chen, S. H. Wei and Y. P. Feng, *J. Am. Chem. Soc.*, 2012, **134**, 17286–17290; (b) E. Pardo, C. Train, G. Gontard, K. Boubekeur, O. Fabelo, H. Liu, B. Dkhil, F. Lloret, K. Nakagawa, H. Tokoro, S.-I. Ohkoshi and M. Verdager, *J. Am. Chem. Soc.*, 2011, **133**, 15328–15331; (c) Z. M. Duan, Y. Zhang, B. Zhang and D. B. Zhu, *J. Am. Chem. Soc.*, 2009, **131**, 6934–6935.
- 14 (a) H. B. Cui, K. Takahashi, Y. Okano, Z. M. Wang, H. Kobayashi and A. Kobayashi, *Angew. Chem., Int. Ed.*, 2005, **44**, 6508; (b) H. B. Cui, Z. M. Wang, K. Takahashi, Y. Okano, H. Kobayashi and A. Kobayashi, *J. Am. Chem. Soc.*, 2006, **128**, 15074–15075.
- 15 H. B. Cui, B. Zhou, L. S. Long, Y. Okano, H. Kobayashi and A. Kobayashi, *Angew. Chem., Int. Ed.*, 2008, **47**, 3376–3380.
- 16 P. Jain, N. S. Dalal, B. H. Toby, H. W. Kroto and A. K. Cheetham, *J. Am. Chem. Soc.*, 2008, **130**, 10450–10451.
- 17 G. C. Xu, X. M. Ma, L. Zhang, Z. M. Wang and S. Gao, *J. Am. Chem. Soc.*, 2010, **132**, 9588–9590.
- 18 P. Jain, V. Ramachandran, R. J. Clark, H. D. Zhou, B. H. Toby, N. S. Dalal, H. W. Kroto and A. K. Cheetham, *J. Am. Chem. Soc.*, 2009, **131**, 13625–13627.
- 19 G. C. Xu, W. Zhang, X. M. Ma, Y. H. Chen, L. Zhang, H. L. Cai, Z. M. Wang, R. G. Xiong and S. Gao, *J. Am. Chem. Soc.*, 2011, **133**, 14948–14951.
- 20 C. Pan, J. P. Nan, X. L. Dong, X. M. Ren and W. Q. Jin, *J. Am. Chem. Soc.*, 2011, **133**, 12330–12333.
- 21 M. D. Segall, P. J. D. Lindan, M. J. Probert, C. J. Pickard, P. J. Hasnip, S. J. Clark and M. C. Payne, *J. Phys.: Condens. Matter*, 2002, **14**, 2717–2744.
- 22 J. P. Perdew, K. Burke and M. Ernzerhof, *Phys. Rev. Lett.*, 1996, **77**, 3865–3868.